catalysts

MDPI

Article

Atmospheric and Efficient Selective Oxidation of Ethylbenzene Catalyzed by Cobalt Oxides Supported on Mesoporous Carbon Nitride

Ye Zhu, Xue-Wen Zhang, Fei Wang, Bing Xue * and Jie Xu *

Jiangsu Key Laboratory of Advanced Catalytic Materials and Technology, School of Petrochemical Engineering, Changzhou University, Gehu Middle Road 21, Changzhou 213164, China

* Correspondence: xuebing@cczu.edu.cn (B.X.); jiexu@cczu.edu.cn (J.X.); Tel.: +86-519-86330135 (B.X. & J.X.)

Abstract: Mesoporous carbon nitride (mpg-C_3N_4) was prepared by using cyanamide as a precursor and colloidal nanosilica as a template. Then, the mpg-C_3N_4 was used as a catalytic support to load CoO_x. The physicochemical properties of the synthesized CoO_x/mpg-C_3N_4 materials were elucidated by multiple characterization methods, and the catalytic activities were examined in the selective oxidation of ethylbenzene (EB) under atmospheric pressure by using *tert*-butyl hydrogen peroxide (TBHP) as an oxidant. It was found that mpg-C_3N_4 possessed a higher specific surface area than other carbon nitride materials, and its abundant N_b species were able to interact with Co (II) species. When the dosages of EB and TBHP were 10 mmol and 30 mmol, respectively, the reaction temperature was 100 °C, and the reaction time was 10 h, the conversion rate of ethylbenzene was 62%, and the selectivity of AP was 84.7%.

Keywords: carbon nitride (C_3N_4); mesoporous material; cobalt oxide; selective oxidation; ethylbenzene

check for updates

Citation: Zhu, Y.; Zhang, X.-W.; Wang, F.; Xue, B.; Xu, J. Atmospheric and Efficient Selective Oxidation of Ethylbenzene Catalyzed by Cobalt Oxides Supported on Mesoporous Carbon Nitride. *Catalysts* **2023**, *13*, 828. https://doi.org/10.3390/catal13050828

Academic Editors: Zhenfeng Bian, Kangle Lv, Sónia Carabineiro and Zeai Huang

Received: 29 March 2023
Revised: 23 April 2023
Accepted: 28 April 2023
Published: 30 April 2023

1. Introduction

Liquid-phase selective oxidation of arenes is one of the most significant strategies for the synthesis of aromatic compounding, including aromatic alcohols, aldehydes, ketones, acids, etc. [1]. From the viewpoints of both fundamental research and industrial application, it is of great interest to develop an efficient and highly selective route for selective oxidation reactions [2]. Among these products, acetophenone (AP) is the simplest aromatic ketone and is widely used to manufacture pharmaceuticals, resins, drugs, perfumes, aldehydes, flavoring agents, etc. Conventionally, AP is produced as a byproduct in the decomposition of cumene hydroperoxide. The Friedel–Crafts acylation reaction, using acid halides or anhydrides in the presence of Lewis acids, is also a well-established process for the production of AP. However, these two processes are environmentally harmful because of the generation of a large amount of corrosive waste [3].

Alternatively, liquid-phase direct oxidation of ethylbenzene (EB) is a practical approach for the synthesis of AP. By now, the most widely reported oxidants include molecular oxygen (O_2), hydrogen peroxide (H_2O_2), and *tert*-butyl hydroperoxide (TBHP). Although O_2 is widely available and inexpensive, the oxidative reaction in the use of O_2 always demands high temperatures and pressures. The use of H_2O_2 can enable the reaction to proceed under atmospheric pressure. However, the low conversion of EB is still a practical issue [4,5]. By comparison, adopting TBHP as an oxidant is a preferable method for the synthesis of AP as the process can be conducted under milder reaction conditions and also offer relatively higher productivity of AP [5].

Until now, the catalysts reported for the TBHP-involved oxidation in the synthesis of AP are mainly supported by Cu (II) [2], Co (II) [1], Cr (III) [6], Ag (I) [7], Pd (II) [8] compounds, etc. Despite their convenience in catalyst separation and product purification, the catalyst supports are mainly silica (or mesoporous silica) and pure carbon materials.

Due to the low interaction, the supported metal species might separate from the catalyst support, and thus, leach out into the liquid phase [9,10]. In this sense, it is of interest to explore a new material as catalyst support, which not only has a large surface area but can also anchor the active metal components in the catalytic reactions.

Graphitic carbon nitride (g-C_3N_4) is a novel inorganic material, which because of its combination of multiple unique physicochemical properties, is widely used in photocatalysis [11,12], fuel cell [13], gas storage [14], etc. In the field of thermal catalysis, owing to its abundant nitrogen-containing groups, g-C_3N_4, especially mesoporous g-C_3N_4 with a large surface area, has been widely reported to be capable of dispersing and anchoring many metal species including K [15,16], Zn [17,18], Co [19,20], Au [21], Pd [22,23], etc. Therefore, g-C_3N_4 material has been regarded as a promising catalytic support in metal-catalyzed heterogeneous reactions [8]. Given the shortcomings in the use of the traditional catalyst supports, in this work, mesoporous carbon nitride (mpg-C_3N_4) was prepared by a hard-templating method, and then, utilized as a support to load cobalt oxide. The synthesized CoO_x/mpg-C_3N_4 materials as heterogeneous catalysts showed good and stable catalytic activity in the selective oxidation of EB to AP by TBHP. The characterization results revealed that there was a possible interaction between Co (II) and the nitrogen-containing species of mpg-C_3N_4.

2. Results and Discussions

2.1. Materials Characterization

Figure 1 shows XRD patterns of mpg-C_3N_4 and 3CoO_x/mpg-C_3N_4-*T* materials. The mpg-C_3N_4 support has two obvious diffraction peaks at 2 θ of 12.7° and 27.6°, indexed as the intralayer and interlayer structure of graphite-like material, i.e., the (100) and (002) planes [24]. The positions of the two peaks show no obvious change from mpg-C_3N_4 and 3CoO_x/mpg-C_3N_4-*T*, while the intensities of the two peaks become weaker because the mpg-C_3N_4 material was prepared by thermal condensation of cyanamide and contains a certain amount of incomplete condensed nitrogen-containing species [25,26]. During the preparation procedure of CoO_x/mpg-C_3N_4, the mpg-C_3N_4 support suffered a second heating treatment, in which the incomplete condensed nitrogen-containing species would decompose into small-molecule gases, such as NH_3. The generated gas inevitably deteriorated the graphic structure of mpg-C_3N_4, thus, leading to the decline of peak intensity in XRD patterns. Nevertheless, the comparison of XRD patterns of mpg-C_3N_4 and 3CoO_x/mpg-C_3N_4-*T* materials suggests that the incorporation of CoO_x has not altered the overall graphitic structures of the mpg-C_3N_4 support. Furthermore, no additional peaks were detected, implying that the supported CoO_x species might disperse better on the surface of mpg-C_3N_4.

The N_2 adsorption–desorption isothermal curves of mpg-C_3N_4 and 3CoO_x/mpg-C_3N_4-*T* materials are described in Figure 2A. The mpg-C_3N_4 material exhibited a typical type-IV isothermal curve, along with an H3 hysteresis loop in the range of relative pressure (p/p_0) = 0.6–0.95, indicating that the mpg-C_3N_4 material possesses mesoporous structures. Similar to mpg-C_3N_4, the supported 3CoO_x/mpg-C_3N_4-*T* materials also have type-IV isothermal curves. The adsorption quantity of such 3CoO_x/mpg-C_3N_4-0.6-*T* materials is associated with the preparation temperature. Among them, 3CoO_x/mpg-C_3N_4-400 possesses the highest adsorption quantity, i.e., the largest total pore volume. The corresponding pore size distributions (Figure 2B) indicate that the pore sizes of both mpg-C_3N_4 and 3CoO_x/mpg-C_3N_4-*T* materials are centered at ca. 12 nm, which is in agreement with the mean particle size (~12 nm) of the Ludox silica template. This suggests that by using the hard-templating procedure, the mpg-C_3N_4-0.6 material has successfully negatively replicated the structure of the silica nanoparticles.

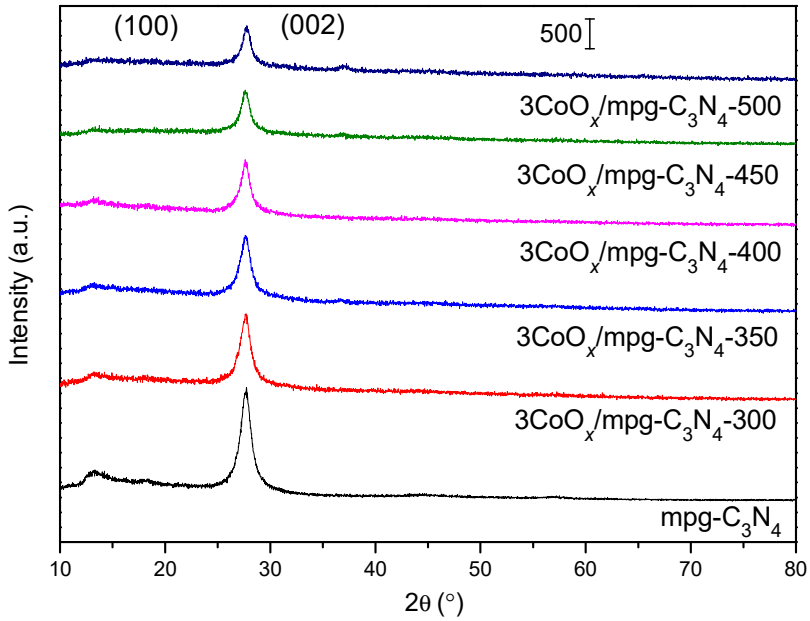

Figure 1. XRD patterns of mpg-C_3N_4 and $3CoO_x$/mpg-C_3N_4-*T* materials.

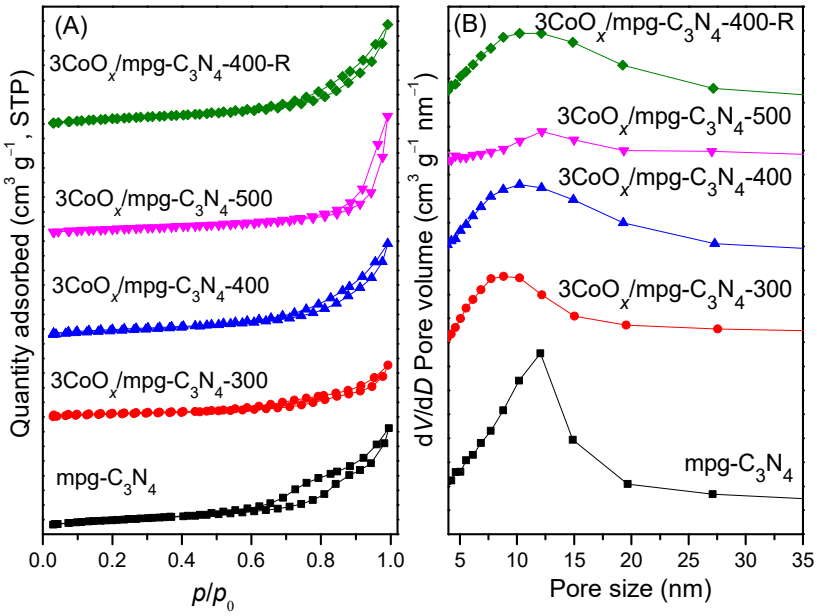

Figure 2. N_2 adsorption–desorption isotherms (**A**) of mpg-C_3N_4 and $3CoO_x$/mpg-C_3N_4-*T* materials and the corresponding pore size distributions (**B**).

Table 1 lists the specific surface area and porous properties of the above materials. The surface area (S_{BET}) of mpg-C_3N_4 is 84 $m^2 \cdot g^{-1}$, and the pore volume is 0.30 $cm^3 \cdot g^{-1}$. For the $3CoO_x$/mpg-C_3N_4-*T* materials, which were prepared by heating treatment of mpg-C_3N_4 and $Co(NO_3)_2$, in addition to the generation of CoO_x from $Co(NO_3)_2$, the mpg-C_3N_4 support also suffers second calcination. Wherein, a slightly higher temperature could induce the decomposition of the skeleton of C_3N_4 of mpg-C_3N_4, which is responsible for the larger surface area and pore volume of $3CoO_x$/mpg-C_3N_4-400 than $3CoO_x$/mpg-C_3N_4-300. However, an extra high heating temperature might induce the partial collapse of the mesoporous structures.

Table 1. Specific surface areas and porous properties of mpg-C_3N_4 and $3CoO_x$/mpg-C_3N_4-*T* materials.

Sample	S_{BET} ($m^2 \cdot g^{-1}$)	Pore Size (nm) [a]	Pore Volume ($cm^3 \cdot g^{-1}$)	Mass (g) [b]
mpg-C_3N_4	84	13.2	0.30	2.44
$3CoO_x$/mpg-C_3N_4-300	44	8.8	0.15	0.57
$3CoO_x$/mpg-C_3N_4-350	32	10.2	0.15	0.53
$3CoO_x$/mpg-C_3N_4-400	70	10.2	0.26	0.45
$3CoO_x$/mpg-C_3N_4-450	56	10.5	0.87	0.35
$3CoO_x$/mpg-C_3N_4-500	60	12.5	0.32	0.24
$3CoO_x$/mpg-C_3N_4-400-R	77	12.1	0.28	–

[a] Determined by the adsorption branches. [b] Mass of the synthesized materials.

The microscopic morphology of the materials was analyzed by SEM (Figure 3). The image of mpg-C_3N_4 revealed coral-like morphology. In the case of $3CoO_x$/mpg-C_3N_4, the SEM image also exhibited a coral-like structure, whereas directly judging the image images, the particles of $3CoO_x$/mpg-C_3N_4 look much smaller than those of mpg-C_3N_4. The energy dispersive X-ray spectroscopy (EDX) mapping (Figure 4) of $3CoO_x$/mpg-C_3N_4 indicates that carbon, nitrogen, oxygen, and cobalt elements are evenly distributed in this material.

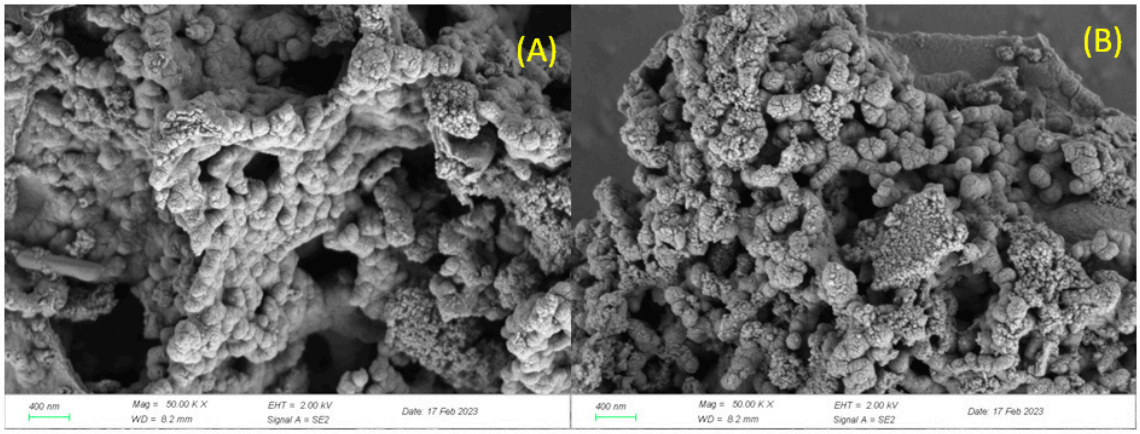

Figure 3. SEM images of mpg-C_3N_4 (**A**) and $3CoO_x$/mpg-C_3N_4 (**B**).

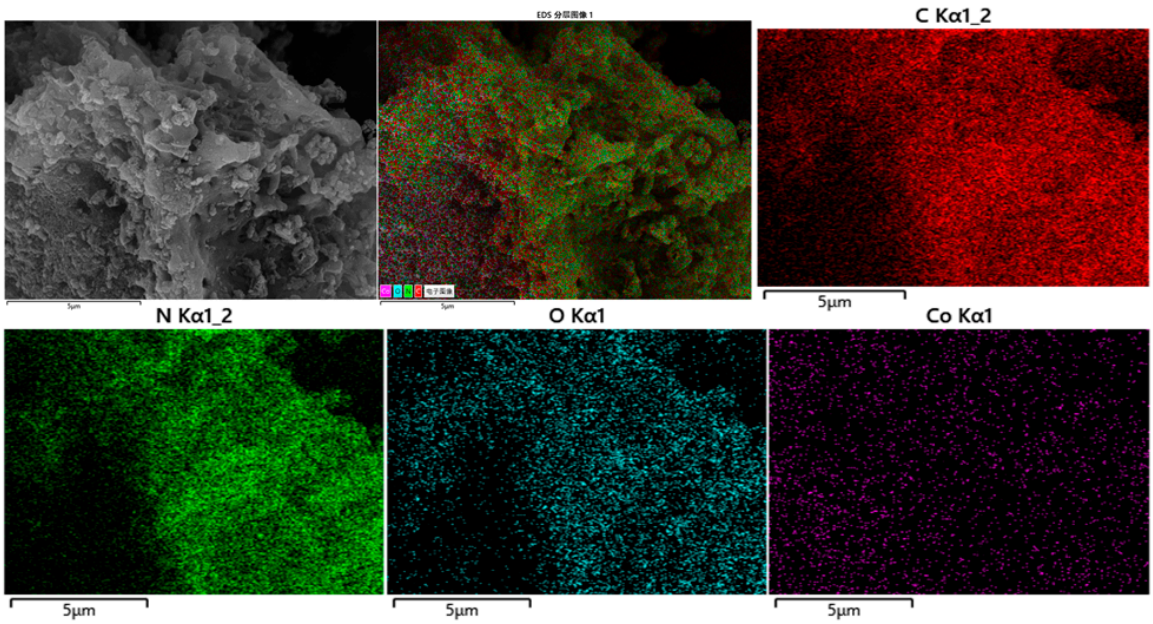

Figure 4. EDX mapping of $3CoO_x$/mpg-C_3N_4.

TEM was used to further analyze the microscopic morphology of the mpg-C_3N_4 and 3CoO_x/mpg-C_3N_4 materials. As displayed in Figure 5, mpg-C_3N_4 features disordered foam-like pores (especially at the edge of the particles) with diameters in a range of 10–15 nm, similar to the reported mesoporous g-C_3N_4 samples prepared using nanoparticles as hard templates [26,27]. These TEM images, in conjunction with the results of the N_2 adsorption–desorption (Table 1), provide evidence that the disordered mesoporous structure of mpg-C_3N_4 is the negative replica of the silica templates. The image of the 3CoO_x/mpg-C_3N_4 also reveals a disordered foam-like porous structure, some of which, however, seem to be blocked and aggregated. As described above, this is due to the collapse of the mesostructures of mpg-C_3N_4 during its second calcination. The CoO_x particles are found on the surface of mpg-C_3N_4. Rough statistics show that the mean size of these CoO_x particles is ca. 15 nm (Figure S1).

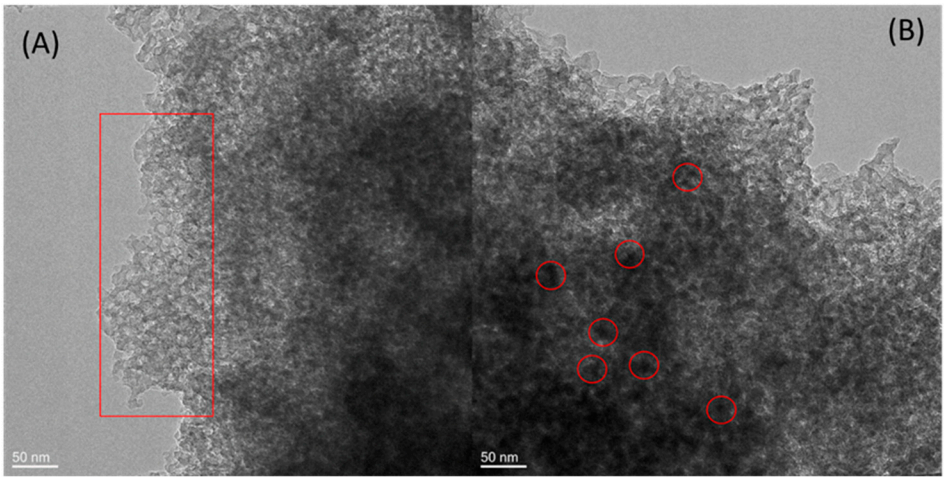

Figure 5. TEM images of mpg-C_3N_4 (**A**) and 3CoO_x/mpg-C_3N_4 (**B**).

The chemical functionalities of mpg-C_3N_4 and the supported materials were analyzed by FT-IR spectroscopy (Figure S2). The spectra of all the materials exhibit sharp and strong transmittance peaks centered ca. 812 cm^{-1}, characteristic bands corresponding to the breathing mode of conjugated heptazine units [26]. The multiple bands in the range of 1200–1600 cm^{-1} are attributed to the stretching vibration of the C–N and C=N groups in the heterocyclic compounds. In addition, a broad band is detected at ca. 3152 cm^{-1} in each material. This transmittance signal is ascribed to the O–H groups in the adsorbed water and the amino group in mpg-C_3N_4. The above bands in the three regions are characteristic of g-C_3N_4. Comparing all the spectra from the 3CoO_x/mpg-C_3N_4 materials with various preparation temperatures and loading amounts (Figure S3) of CoO_x, no additional bands were observed, suggesting that the loading of CoO_x has not changed the overall chemical functionalities of mpg-C_3N_4.

The surface chemical bonding state was probed by XPS analysis. Figure 6 is the survey spectra of mpg-C_3N_4 and 3CoO_x/mpg-C_3N_4-*T* materials. Three peaks appear at the binding energies of ca. 288, 398, and 531 eV, which signify the carbon, nitrogen, and oxygen elements, respectively. In the cases of the 3CoO_x/mpg-C_3N_4-*T* materials, in addition to the three peaks, peaks were detected at ca. 781 eV, indexed as Co 2p orbits. Based on the peak areas, the molar ratios of carbon to nitrogen in the materials were calculated. As listed in Table S1, the molar ratio obtained from mpg-C_3N_4 was 0.85:1, much higher than the theoretical value of ideal g-C_3N_4 (0.75:1) [24]. Compared to the bulk g-C_3N_4, prepared without templating procedure, the C_3N_4 wall of mpg-C_3N_4 was much thinner; thus, resulting in an easier decomposition of the nitrogen-containing groups during the heating step of mpg-C_3N_4 [27]. As for the 3CoO_x/mpg-C_3N_4-*T* materials, the molar ratios of carbon to nitrogen are close to the value of mpg-C_3N_4.

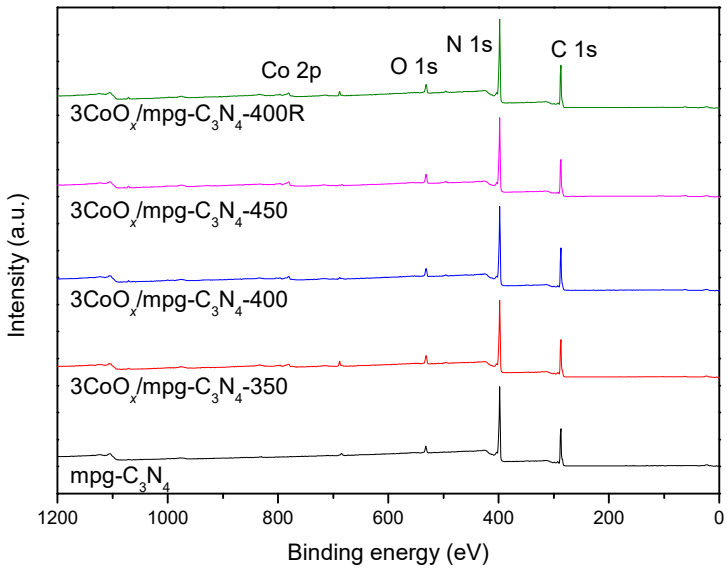

Figure 6. XPS survey of mpg-C_3N_4 and $3CoO_x$/mpg-C_3N_4-*T* materials.

As described above, supported Co materials have recently been widely studied as heterogeneous catalysts in the selective oxidation of EB, and therein, the chemical bonding state of cobalt species is an important factor in deciding the catalytic performance [28]. Given this point, the fine Co $2p_{3/2}$ spectra of $3CoO_x$/mpg-C_3N_4-*T* were deconvoluted (note: the deconvolution of Co $2p_{1/2}$ spectra was not performed as the corresponding peaks were very weak). As illustrated in Figure 7, the Co $2p_{3/2}$ signals can be separated into four peaks. The peaks with binding energies of ca. 780.4 and 785.2 eV are assigned to Co (III) and Co (II), respectively [9,29,30]. The weak peaks centered at ca. 788.2 eV are attributed to shake-up (satellite) signals in the Co $2p_{3/2}$ orbit [31,32], and the low-intensity signals in the range of 774–778 eV are attributed to Co^0. Such metallic cobalt species could come from the reduction of cobalt cations by some nitrogen-containing species of mpg-C_3N_4 during the preparation procedure (i.e., heating treatment), which has also been reported in cobalt supported by nitrogen-doped carbon materials [33,34].

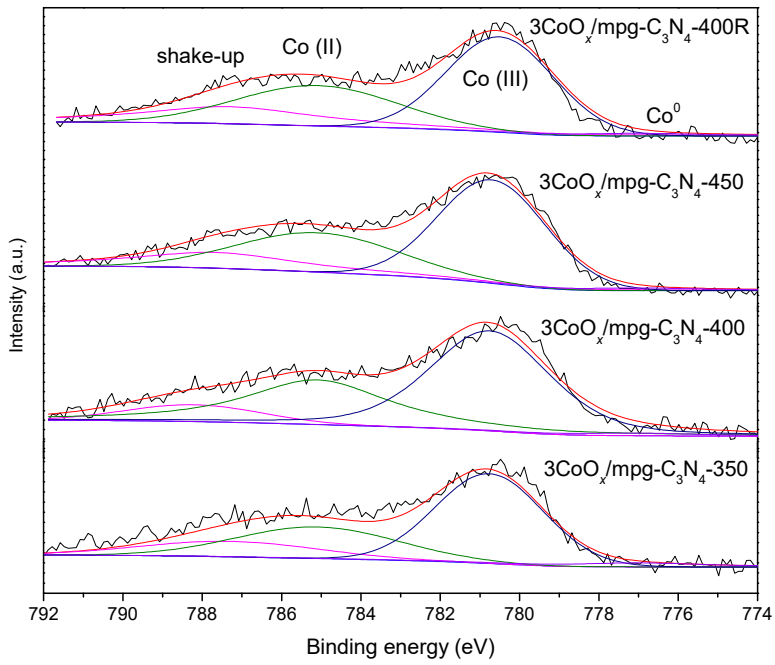

Figure 7. Co $2p_{3/2}$ fine spectra of $3CoO_x$/mpg-C_3N_4-*T* materials.

On the other hand, g-C_3N_4 and its derived materials contain abundant nitrogen-containing groups and particular nitrogen pots surrounded by nonbonding sp^2 orbitals of nitrogen atoms [35]. Comparable to porphyrin and phthalocyanine, such unique structures enable g-C_3N_4 and its related materials to be able to include metal species [18]. In view of this point, the fine N 1s spectra of various materials were analyzed and presented in Figure 8. The spectra of mpg-C_3N_4 and 3CoO_x/mpg-C_3N_4-*T* are deconvoluted into three independent peaks. The major peaks with the lowest binding energies of 397.8 eV are attributed to sp^2-hybridized nitrogen atoms (N_a) in the conjugated heptazine units. This type of nitrogen accounts for over 65% of the total nitrogen species. The peaks at 398.9 and 400.2 eV correspond to bridging nitrogen atoms (N_b) that connect several adjacent heptazine units, and incomplete uncondensed amino groups (–NH_2 and –NH–, N_c), respectively [26,36]. Accordingly, the distributions of various nitrogen species in the materials were calculated (Table 2). It can be found that the introduction of CoO_x affects the distribution of the nitrogen groups, leading to the transformation of a small number of N_a to N_b species. The variation is probably derived from the partial destruction of the heptazine rings (N_a) in mpg-C_3N_4, which occurs in the preparation steps of 3CoO_x/mpg-C_3N_4-*T* and has actually been reported in previous literature about metal-included g-C_3N_4 materials [37,38]. Moreover, among the three 3CoO_x/mpg-C_3N_4-*T* materials, 3CoO_x/mpg-C_3N_4-400 owns the highest percentage of N_b (25.5%). It should be noted that such a type of nitrogen has a superior capacity to N_a and N_c when interacting with a transition-metal cation [39]; thus, probably facilitating the dispersion of Co species in the mpg-C_3N_4 support.

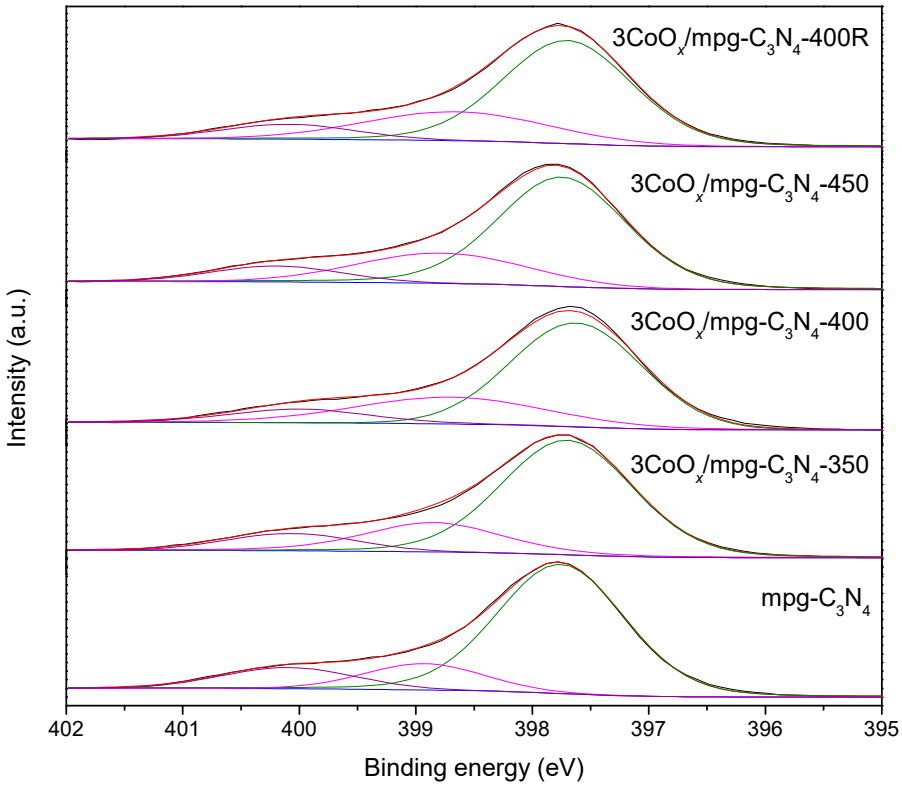

Figure 8. N 1s fine spectra of mpg-C_3N_4 and 3CoO_x/mpg-C_3N_4-*T* materials.

The interaction between Co and mpg-C_3N_4 has also been evidenced by the UV–vis spectra. As depicted in Figure S4, the spectrum of the mpg-C_3N_4 material displays photo-absorption in the UV region, ascribed to the bandgap between HOMO and LUMO in the polymeric heptazine units of g-C_3N_4. The spectra of 3CoO_x/mpg-C_3N_4-*T* materials show similar absorption intensities in the UV region to the support. Notwithstanding, compared with mpg-C_3N_4, the supported materials demonstrate enhanced absorption in the visible light region. Such a variation in the electronic structure of mpg-C_3N_4 is attributed to the

inclusion of the metal cation in the framework of g-C_3N_4, i.e., d–p repulsion between N 2p and Co 3d orbits, which has also been found in metal-doped g-C_3N_4 materials [18,40–42]. Moreover, in the cases of CoO_x/mpg-C_3N_4 materials with various loading amounts of CoO_x, it can be found that as the loading amount is increased, the increase in the absorption intensity in the visible region becomes more obvious. In fact, the change in the electronic structure has also been reflected by the apparent colors of the materials. The color of mpg-C_3N_4 is pale yellow, whereas the 3CoO_x/mpg-C_3N_4 materials are green. Combining the analytic results of UV–vis and XPS spectra, it can be further induced that the Co species could interact with the mpg-C_3N_4 materials. Namely, the loading of CoO_x onto mpg-C_3N_4 is not merely via physical dispersion.

Table 2. Molar percentages of various cobalt and nitrogen species [a].

Material	Co (II)	Co (III)	Co^0	N_a	N_b	N_c
mpg-C_3N_4	–	–	–	74.1	14.0	11.9
3CoO_x/mpg-C_3N_4-350	32.7	62.0	5.3	70.1	20.1	9.8
3CoO_x/mpg-C_3N_4-400	41.5	56.0	2.4	64.8	25.5	9.7
3CoO_x/mpg-C_3N_4-450	35.3	61.6	3.1	68.0	22.9	9.1
3CoO_x/mpg-C_3N_4-400R	37.6	59.2	3.2	66.0	24.9	9.1

[a] Calculated by deconvoluted Co $2p_{3/2}$ and N 1s spectra.

2.2. Catalyst Activity

The above materials were evaluated in the selective oxidation of EB using TBHP as an oxidant and acetonitrile as a solvent (Table 3). In the blank test without any catalysts, only 1.6% of EB is converted. The major product, BA accounting for 55.9%, originated from the deep oxidation of AP. After the addition of 100 mg of 3CoO_x/g-C_3N_4, the conversion of EB is drastically improved, and the AP becomes the main product. Compared with 3CoO_x/g-C_3N_4, 3CoO_x/eg-C_3N_4 exhibits higher catalytic activity. Obviously, the supported CoO_x is the key site in this selective oxidation and the eg-C_3N_4 support with the large surface area could facilitate the exposure of more catalytic sites. Besides g-C_3N_4 and eg-C_3N_4, the CoO_x catalysts supported on carbon nanotube (CNT) and ordered mesoporous silica FDU-12 have also been prepared and examined under the same reaction conditions. Unfortunately, the corresponding conversions of EB and selectivity to AP are all less than the values gained in 3CoO_x/eg-C_3N_4.

Table 3. Catalytic performances of various catalysts in the selective oxidation of EB [a].

Catalyst	Con. (%)	Sel. (%)		
		AP	PE	BA
/	1.6	26.6	17.5	55.9
3CoO_x/g-C_3N_4	27.6	75.2	14.5	10.3
3CoO_x/eg-C_3N_4	32.9	74.6	9.5	15.9
3CoO_x/CNT	19.6	63.5	18.8	17.7
3CoO_x/FDU-12	8.6	71.9	11.2	16.9
3CoO_x/mpg-C_3N_4-0.4	37.8	79.4	6.8	13.8
3CoO_x/mpg-C_3N_4-0.6	62.0	84.7	4.8	10.6
3CoO_x/mpg-C_3N_4-0.8	57.4	83.6	5.2	11.8
3CoO_x/mpg-C_3N_4-1.2	35.9	75.5	15.2	9.3
3CoO_x/mpg-C_3N_4-0.6 [b]	10.7	67.8	27.1	5.1
3CoO_x/mpg-C_3N_4-0.6-R	60.3	81.2	5.9	12.9

[a] Reaction conditions: 10 mmol of EB, 30 mmol of TBHP, $W_{catal.}$ = 100 mg, 4 mL of acetonitrile, T = 100 °C, and t = 10 h. [b] Reaction conditions: 10 mmol of EB, O_2 (10 mL·min^{-1}), $W_{catal.}$ = 100 mg, 4 mL of acetonitrile, T = 120 °C, and t = 10 h.

By contrast, the use of mpg-C_3N_4 supports the results of higher catalytic activity than eg-C_3N_4. Moreover, in the cases of 3CoO_x/mpg-C_3N_4 catalysts, the EB conversions are

found to be related to the supports. Among them, $3CoO_x$/mpg-C_3N_4-0.6 and $3CoO_x$/mpg-C_3N_4-0.8 demonstrate superior activity to $3CoO_x$/mpg-C_3N_4-0.4 and $3CoO_x$/mpg-C_3N_4-1.2. The obtained maximum conversion of EB is 62.0%, together with 84.7% of AP. The difference between various mpg-C_3N_4 supports is derived by adding the amounts of the siliceous templates (i.e., Ludox HS40). The N_2 adsorption–desorption characterization results (Figure S5) confirm that all the $3CoO_x$/mpg-C_3N_4 catalysts are mesoporous materials, along with the relatively concentrated pore size distributions of ca. 10 nm. As listed in Table S2, both the surface areas and pore volumes of $3CoO_x$/mpg-C_3N_4-0.6 and $3CoO_x$/mpg-C_3N_4-0.8 are larger than those of the other two materials, probably responsible for their higher catalytic activities. Additionally, we evaluated the catalytic activity of $3CoO_x$/mpg-C_3N_4-0.6 using molecular oxygen as an oxidant instead of TBHP. As shown in Table 3, a small amount of EB (10.7%) can be also converted.

In addition to the preparation conditions of the mpg-C_3N_4 support, we have also prepared a series of $3CoO_x$/mpg-C_3N_4 with various heating temperatures (300–500 °C), and the corresponding catalytic performances are summarized in Table 4. It can be seen that the EB conversion and the selectivity to AP increase alongside the elevation of the heating temperature. As revealed in the above XPS analytical results (Table 2), among the several $3CoO_x$/mpg-C_3N_4-*T* (350–450 °C) materials, $3CoO_x$/mpg-C_3N_4-400 has the highest percentage of Co (II) cation and largest surface area. As reported by Jie and Yang et al. [29,43], Co (II) instead of Co (III) is proposed as the crucial catalytic active site in the oxidation of EB. Alongside Co (II), the abundant N_b species are able to anchor Co (II) and restrain its further oxidation. For the $3CoO_x$/mpg-C_3N_4 materials prepared in higher temperatures, the obtained EB conversions are much higher than the values gained by $3CoO_x$/mpg-C_3N_4-400. Nevertheless, it should be noted that due to the high preparation temperature, the masses of the two catalysts were indeed very low (Table 1).

Table 4. Catalytic performances of various $3CoO_x$/mpg-C_3N_4-*T* catalysts in the selective oxidation of EB [a].

Catalyst	Con. (%)	Sel. (%)		
		AP	PE	BA
$3CoO_x$/mpg-C_3N_4-300	11.7	69.2	7.6	23.3
$3CoO_x$/mpg-C_3N_4-350	23.8	69.0	9.1	21.9
$3CoO_x$/mpg-C_3N_4-400	62.0	84.7	4.8	10.6
$3CoO_x$/mpg-C_3N_4-450	71.1	90.0	2.8	7.2
$3CoO_x$/mpg-C_3N_4-500	76.6	91.4	1.8	6.8

[a] Reaction conditions: 10 mmol of EB, 30 mmol of TBHP, $W_{catal.}$ = 100 mg, 4 mL of acetonitrile, T = 100 °C, and t = 10 h.

Table S3 shows the catalytic performances of CoO_x/mpg-C_3N_4 catalysts with various loading amounts of CoO_x. Adopting a high loading amount results in an obvious increase in EB conversion along with selectivity to AP. However, as the loading amount is greater than 5 wt%, no significant improvement in catalytic conversion was received. This might be due to the possible agglomeration of the CoO_x species on the mpg-C_3N_4 support.

The $3CoO_x$/mpg-C_3N_4 catalyst was chosen as a representative to further explore the effect of the reaction conditions on the catalytic performance. As shown in Figure 9A, under a reaction temperature of 80 °C, the EB conversion is only 28.8% and the selectivity to AP is 73.7%. At 120 °C, the conversion could reach 98.6% but the selectivity levels off. As mentioned above, using molecular oxygen instead of TBHP, the corresponding conversion of EB could also reach up to 10.7% (Table 3). The much higher conversion acquired at 120 °C could be due to the corporative oxidation of EB by TBHP and oxygen. The influence of reaction time on the catalytic performance is plotted in Figure 9B. It can be seen that prolonging the reaction could achieve higher catalytic conversions of EB. However, after a reaction of 10 h, the conversion exhibits an equilibrium. That is, as time increases, the conversion does not increase progressively. Figure S6 describes the catalytic performances

with various feeding doses of $3CoO_x$/mpg-C_3N_4. As the weight of the catalyst is greater than 100 mg, the conversion shows no obvious improvement.

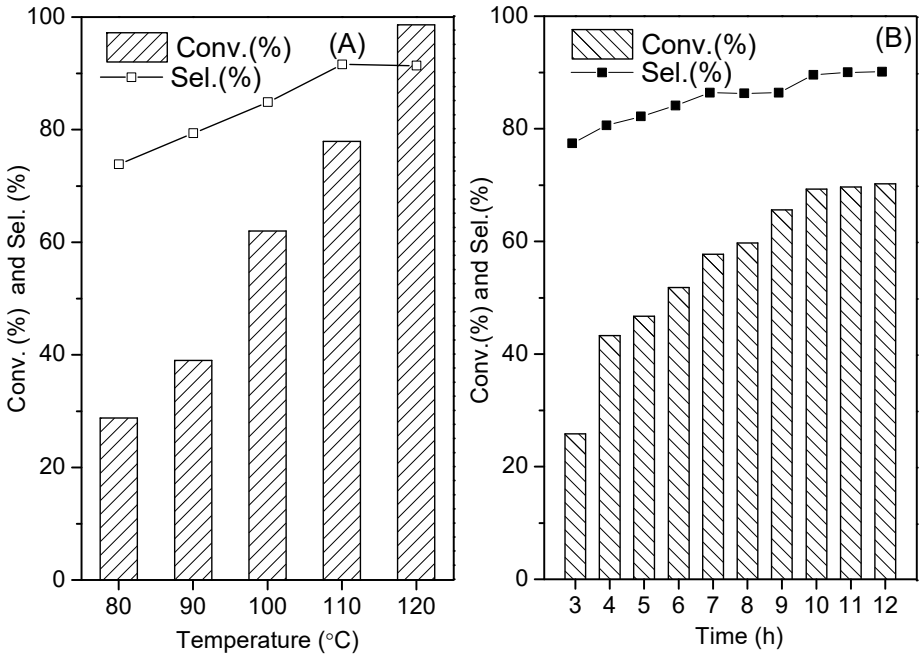

Figure 9. Catalytic performances of $3CoO_x$/mpg-C_3N_4 under various reaction temperatures (**A**) and reaction time (**B**). Reaction conditions: 10 mmol of EB, 30 mmol of TBHP, $W_{catal.}$ = 100 mg, 4 mL of acetonitrile, t = 10 h (**A**), and T = 100 °C (**B**).

The recycling test has also been conducted to test the recyclability of the $3CoO_x$/mpg-C_3N_4. After four consecutive runs, the EB conversion and selectivity to AP are 60.3% and 81.2%, respectively (Table 3). Namely, there is only a slight loss in catalytic activity after several runs. The physicochemical properties of the recycled catalyst were analyzed by N_2 adsorption–desorption and XPS, and the corresponding results confirm that the surface areas (Table 1) and surface chemical compositions (Tables S1 and 2) of the catalyst have not undergone apparent change after the recycling experiments, suggesting good recyclability and stability of the catalyst in the selective oxidation of EB.

Table 5 lists the recently reported catalytic performances of the supported metal catalysts (heterogeneous system) in the selective oxidation of EB to AP by TBHP. The catalytic active metals mainly include Pd, Co, Cu, and Mn. From the viewpoint of reaction conditions, the reaction temperatures are basically in the range of 80–100 °C. Overall, the most efficient catalysts are the supported precious catalysts, which can convert EB smoothly under 80 °C. However, the major shortcoming in the use of such catalysts might be their high cost. For the other metal catalysts, their catalyst supports are mainly functionalized mesoporous materials, including SBA-15 [2], SBA-1 [44], TUD-1 [45], and organometallic-SiO_2/Al_2O_3 [46], where the preparation of these materials requires expensive organic surfactants as soft templates and the whole processes for the final supported catalysts are relatively complicated. In terms of catalytic performance, the 3CoOx/mpg-C3N4 catalyst in this work demonstrates moderate catalytic activity under relatively mild reaction conditions. In this sense, the present work provides a convenient and low-cost heterogeneous catalyst for atmospheric and efficient selective oxidation of EB to AP.

Table 5. Comparison of catalytic performances of supported metal catalysts in selective oxidation of EB by TBHP.

Catalyst	n_{TBHP} (mmol)	n_{EB} (mmol)	$W_{catal.}$ (mg)	T (°C)	t (h)	Conv. (%)	Sel. (%)
Pd/g-C_3N_4–rGO [8]	4	1	10	80	24	67	97
Pd/CeO_2 [47]	1	1	20	80	4	100	79
Co-Cu/SAPS-15 [2]	30	10	30	100	6	97	100
MnSBA-1 [44]	10		100	80	8	20	57
CoTUD-1 [45]	10	10	100	80	8	38	74
SiO_2/Al_2O_3-APTMS [46]	9	9	50	50	24	27	74
LDH-[NAPABA–Cu(II)]	39	13	100	120	7	81	100
3CoO_x/mpg-C_3N_4	30	10	100	100	10	62	85

3. Experimental Section

3.1. Catalyst Preparation

3.1.1. Synthesis of Mpg-C_3N_4

Mesoporous C_3N_4 materials were prepared according to the previous hard-templating approach reported by Goettmann et al. [48]. In brief, 4 g of cyanamide was added to 4–12 g of a colloidal silica particle (~12 nm) dispersion (Ludox HS40, 40 wt%, Sigma-Aldrich, Shanghai, China), stirred for 2 h, and ultrasonicated for 20 min. The mixture was heated at 60 °C until completely dried. Next, the white solid was ground, transferred into a crucible with a lid, heated with a ramping rate of 2.5 °C·min^{-1} to reach 550 °C, and tempered for this temperature for another 3 h. The obtained pale-yellow powder was labeled as mpg-C_3N_4-SiO_2.

Mpg-C_3N_4-SiO_2 was added to 200 mL of NH_4HF_2 (Aladdin, Shanghai, China) aqueous solution (4 mol·L^{-1}) and stirred at room temperature for 24 h to remove the silica template. After that, the suspension was filtrated and rinsed with water several times until the pH value of the supernatant was close to 7. The obtained yellow solid was further rinsed with ethanol two times, and dried overnight at 60 °C. The resultant solid was designated as mpg-C_3N_4-*r*, where *r* indicated the ratio of silica in Ludox to cyanamide.

3.1.2. Preparation of CoO_x/Mpg-C_3N_4

Mpg-C_3N_4 (600 mg) was added to 20 mL of cobalt nitrate aqueous solution containing 30–207 mg of $Co(NO_3)_2{\cdot}6H_2O$ (Aladdin, Shanghai, China). The suspension was ultrasonicated for 30 min, stirred for 3 h, and heated with stirring to 80 °C, until completely dried. The obtained, orange-colored solid was ground, transferred into a silica boat in a tubular furnace with N_2 flow (ca. 20 mL·min^{-1}), and heated at a rate of 3 °C·min^{-1} to a desired temperature (300–500 °C), and then, tempered at the temperature for another 3 h. The resultant dark green powder was labeled as *m*CoO_x/mpg-C_3N_4-*r*-*T*, where *r* and *T* indicated the loading amount of Co and heating temperature, respectively. Unless otherwise specified, *r* and *T* were 0.6 and 400, respectively.

3.1.3. Preparation of Other Supported CoO_x Catalysts

Similar to the preparation procedure of CoO_x/mpg-C_3N_4, other supported CoO_x catalysts were prepared by using exfoliated g-C_3N_4 (eg-C_3N_4), carbon nanotube, and ordered mesoporous FDU-12 as catalytic supports. The preparation methods of eg-C_3N_4 and FDU-12 are described in the supplementary material.

3.2. Material Characterization

The specific surface areas and porous properties of the materials were analyzed by N_2 adsorption–desorption isotherms at −196 °C using an ASAP 2020 (Micromeritics, Norcross, GA, US) instrument. Before the analysis, the samples were pretreated in a vacuum at 150 °C for 6 h. The surface areas were calculated using the Brunauer–Emmet–Teller (BET) method.

X-ray diffraction (XRD) patterns were recorded on a D/max 2500 X-ray diffractometer (Rigaku, Tokyo, Japan) using a graphite monochromator (40 kV, 40 mA) equipped with Ni-filtered Cu-$K\alpha$ radiation.

Fourier-transform infrared (FT-IR) spectra were tested in a Tensor 27 (Bruker, Billerica, MA, US) spectrometer based on the transmission mode with a resolution of 4 cm^{-1}. Each spectrum was based on 32 scans (4000–400 cm^{-1}).

UV–vis diffuse reflectance spectra were carried out on a UV-3600 spectrophotometer (Shimadzu, Tokyo, Japan) using $BaSO_4$ as a standard reference.

X-ray photoelectron spectroscopy (XPS) measurements were performed using an ESCALAB 250 XI spectrometer (Thermo–Fisher, Waltham, MA, US) working in a constant energy mode with Mg K_α radiation as the excitation source.

Scanning electron microscopy (SEM) images were obtained on a Gemini SEM 300 (ZEISS, Oberkochen, Germany) microscope.

Transmission electron microscopy (TEM) experiments were conducted with a Talos F200X G2 (FEI, Hillsboro, OR, USA) electron microscope.

3.3. Catalytic Evaluation

The atmospheric selective oxidation of EB was carried out in a three-necked round-bottom flask equipped with a condenser. EB (10 mmol) and acetonitrile (4 mL) were mixed well, followed by the addition of 100 mg of catalyst. After the mixture was heated up to 100 °C, under continuous stirring (500 rpm), 30 mmol of TBHP (70 wt%, a.q.) was added into the flask through a peristaltic pump (the feeding time lasted for ca. 30 min). The reaction proceeded for 1–12 h. During the process, a small amount of reaction mixture (ca. 0.1 mL) was collected periodically and centrifuged. The liquid phase was analyzed by a gas chromatograph (Shangdong Rainbow Chemical Co., Ltd., Zaozhuang, China) equipped with a capillary column (FFAP). The conversion (conv.) of EB and selectivity (sel.) to AP were calculated using an area-normalization method, and the detailed calculation equations were as follows:

$$Conv.(\%) = \frac{A_{AP} \times f_{AP} + A_{PE} \times f_{PE} + A_{BA} \times f_{BA}}{A_{EB} \times f_{EB} + A_{AP} \times f_{AP} + A_{PE} \times f_{PE} + A_{BA} \times f_{BA}}$$

$$Sel.(\%) = \frac{A_{AP} \times f_{AP}}{A_{AP} \times f_{AP} + A_{PE} \times f_{PE} + A_{BA} \times f_{BA}}$$

where A and f were the peak area and response factor, respectively, for each component analyzed by GC. BA and PE stood for benzaldehyde and phenethyl alcohol, respectively.

4. Conclusions

In summary, mpg-C_3N_4 material was prepared using cyanamide as a precursor and colloidal silica as the template, which was then used as catalyst support to load cobalt oxide (CoO_x). The characterization results show that the mesoporous structures of mpg-C3N4 remained after the incorporation of CoOx. Co (II) species disperse on the surface of the support and there is a probable interaction between Co (II) and the nitrogen species in mpg-C_3N_4. The heating temperatures during the catalyst preparation can adjust the distributions of the Co cations and nitrogen species. In the selective oxidation of EB by TBHP, the $3CoO_x$/mpg-C_3N_4-400 catalyst exhibited higher catalytic activity than other catalysts.

Supplementary Materials: The following supporting information can be downloaded at: https://www.mdpi.com/article/10.3390/catal13050828/s1, Preparation of eg-C_3N_4 and FDU-12; Figure S1: Particle size histogram of CoO_x in $3CoO_x$/mpg-C_3N_4-400; Figure S2: FT-IR spectra of mpg-C_3N_4 (a), $3CoO_x$/mpg-C_3N_4-300 (b), $3CoO_x$/mpg-C_3N_4-350 (c), $3CoO_x$/mpg-C_3N_4-400 (d), $3CoO_x$/mpg-C_3N_4-450 (e), and $3CoO_x$/mpg-C_3N_4-500 (f) materials; Figure S3: FT-IR spectra of $m$$CoO_x$/mpg-$C_3N_4$ materials; Figure S4: UV–vis spectra of mpg-C_3N_4 and CoO_x/mpg-C_3N_4 materials; Figure S5: N_2 adsorption–desorption isotherms (A) of $3CoO_x$/mpg-C_3N_4-r materials and the corresponding pore

size distributions (B); Figure S6: Catalytic performances with various feeding doses of $3CoO_x$/mpg-C_3N_4. Reaction conditions:10 mmol of EB, 30 mmol of TBHP, 4 mL of acetonitrile, T = 100 °C, and t = 10 h; Table S1: Molar ratios of C/N of mpg-C_3N_4 and $3CoO_x$/mpg-C_3N_4-T materials; Table S2: Surface areas and porous properties of $3CoO_x$/mpg-C_3N_4-r materials; Table S3: Catalytic performances of various $m$$CoO_x$/mpg-$C_3N_4$ catalysts in the selective oxidation of EB.

Author Contributions: Conceptualization and methodology, J.X.; writing—original draft preparation, Y.Z.; writing—review and editing, J.X. and B.X.; investigation and test, Y.Z., X.-W.Z. and F.W. All authors have read and agreed to the published version of the manuscript.

Funding: This work was supported by the National Natural Science Foundation of China (21878027).

Data Availability Statement: The data presented in the study are available from the corresponding author.

Acknowledgments: This work was supported by Advanced Catalysis and Green Manufacturing Collaborative Innovation Center.

Conflicts of Interest: The authors declare no conflict of interest.

References

1. Chaudhary, V.; Sharma, S. Study of ethylbenzene oxidation over polymer-silica hybrid supported Co (II) and Cu (II) complexes. *Catal. Today* **2021**, *375*, 601–613. [CrossRef]
2. Chaudhary, V.; Sharma, S. Synthesis of polymer-silica hybrid-supported catalysts for solvent-free oxidation of ethylbenzene with TBHP. *Asia Pac. J. Chem. Eng.* **2020**, *15*, e2441. [CrossRef]
3. Nandanwar, S.U.; Rathod, S.; Bansal, V.; Bokade, V.V. A review on selective production of acetophenone from oxidation of ethylbenzene over heterogeneous catalysts in a decade. *Catal. Lett.* **2021**, *151*, 2116–2131. [CrossRef]
4. Wang, K.; Zhao, S.; Ma, L.; Yang, M.; Qin, J.; Huang, X.; Gong, L.; Xiong, Y.; Li, R. A 3D-honeycomb-like catalyst: A nitrogen-doped carbon material with cobalt and manganese-oxide for C–H bond oxidation. *Inorg. Chem. Front.* **2019**, *6*, 3270–3287. [CrossRef]
5. Liu, J.; Wang, W.; Jian, P.; Wang, L.; Yan, X. Promoted selective oxidation of ethylbenzene in liquid phase achieved by hollow $CeVO_4$ microspheres. *J. Colloid Interface Sci.* **2022**, *614*, 102–109. [CrossRef]
6. Selvaraj, M.; Park, D.W.; Kim, I.; Kawi, S.; Ha, C.S. Highly active mesoporous chromium silicate catalysts in side-chain oxidation of alkylaromatics. *Dalton Trans.* **2012**, *41*, 14204–14210. [CrossRef] [PubMed]
7. Raji, V.; Chakraborty, M.; Parikh, P.A. Catalytic Performance of Silica-Supported Silver Nanoparticles for Liquid-Phase Oxidation of Ethylbenzene. *Ind. Eng. Chem. Res.* **2012**, *51*, 5691–5698. [CrossRef]
8. Nilforoushan, S.; Ghiaci, M.; Hosseini, S.M.; Laurent, S.; Muller, R.N. Selective liquid phase oxidation of ethyl benzene to acetophenone by palladium nanoparticles immobilized on a g-C_3N_4–rGO composite as a recyclable catalyst. *New J. Chem.* **2019**, *43*, 6921–6931. [CrossRef]
9. Li, Y.; Jie, S.; Li, K.; Liu, Z. Synthesis of efficient Co and N co-doped carbon catalysts with high surface areas for selective oxidation of ethylbenzene. *New J. Chem.* **2018**, *42*, 12677–12683. [CrossRef]
10. Zhang, H.; Cai, A.; He, H.; Zhang, Q.; Zhang, F.; Zhang, G.; Fan, X.; Peng, W.; Li, Y. Nitrogen-doped 3D hollow carbon spheres for efficient selective oxidation of C–H bonds under mild conditions. *New J. Chem.* **2022**, *46*, 9727–9734. [CrossRef]
11. Wang, X.; Blechert, S.; Antonietti, M. Polymeric Graphitic Carbon Nitride for Heterogeneous Photocatalysis. *ACS Catal.* **2012**, *2*, 1596–1606. [CrossRef]
12. Wang, Y.; Di, Y.; Antonietti, M.; Li, H.; Chen, X.; Wang, X. Excellent Visible-Light Photocatalysis of Fluorinated Polymeric Carbon Nitride Solids. *Chem. Mater.* **2010**, *22*, 5119–5121. [CrossRef]
13. Chakraborty, I.; Ghosh, N.; Ghosh, D.; Dubey, B.; Pradhan, D.; Ghangrekar, M. Application of synthesized porous graphitic carbon nitride and its composite as excellent electrocatalysts in microbial fuel cell. *Int. J. Hydrogen Energy* **2020**, *45*, 31056–31069. [CrossRef]
14. Wang, P.; Xia, K.; Chen, Y.; Tian, Q.; Xiong, R.; Han, B.; Gao, Q.; Zhou, C.; Yu, D. Acid-assisted synthesis of nitrogen-deficient mesoporous graphitic carbon nitride for hydrogen storage. *Mater. Lett.* **2021**, *301*, 130347. [CrossRef]
15. Wu, M.; Yan, J.; Tang, X.; Zhao, M.; Jiang, Q. Synthesis of Potassium-Modified Graphitic Carbon Nitride with High Photocatalytic Activity for Hydrogen Evolution. *ChemSusChem* **2014**, *7*, 2654–2658. [CrossRef] [PubMed]
16. Guo, Y.; Chen, T.; Liu, Q.; Zhang, Z.; Fang, X. Insight into the Enhanced Photocatalytic Activity of Potassium and Iodine Codoped Graphitic Carbon Nitride Photocatalysts. *J. Phys. Chem. C* **2016**, *120*, 25328–25337. [CrossRef]
17. Chen, D.; Wang, K.; Ren, T.; Ding, H.; Zhu, Y. Synthesis and characterization of the ZnO/mpg-C_3N_4 heterojunction photocatalyst with enhanced visible light photoactivity. *Dalton Trans.* **2014**, *43*, 13105–13114. [CrossRef]
18. Wang, X.; Chen, X.; Thomas, A.; Fu, X.; Antonietti, M. Metal-Containing Carbon Nitride Compounds: A New Functional Organic-Metal Hybrid Material. *Adv. Mater.* **2009**, *21*, 1609–1612. [CrossRef]

19. Ghafuri, H.; Jafari, G.; Rashidizadeh, A.; Manteghi, F. Co^{2+} immobilized on highly ordered mesoporous graphitic carbon nitride (ompg-C_3N_4/Co^{2+}) as an efficient and recyclable heterogeneous catalyst for one-pot tandem selective photo-oxidation/Knoevenagel condensation. *Mol. Catal.* **2019**, *475*, 110491. [CrossRef]
20. Yang, C.; Fu, L.; Zhu, R.; Liu, Z. Influence of cobalt species on the catalytic performance of Co-NC/SiO_2 for ethylbenzene oxidation. *Phys. Chem. Chem. Phys.* **2016**, *18*, 4635–4642. [CrossRef]
21. Chen, Z.; Mitchell, S.; Vorobyeva, E.; Leary, R.K.; Hauert, R.; Furnival, T.; Ramasse, Q.M.; Thomas, J.M.; Midgley, P.A.; Dontsova, D.; et al. Stabilization of Single Metal Atoms on Graphitic Carbon Nitride. *Adv. Funct. Mater.* **2017**, *27*, 1605785. [CrossRef]
22. Gong, Y.; Zhang, P.; Xu, X.; Li, Y.; Li, H.; Wang, Y. A novel catalyst Pd@ompg-C_3N_4 for highly chemoselective hydrogenation of quinoline under mild conditions. *J. Catal.* **2013**, *297*, 272–280. [CrossRef]
23. Yi, X.-T.; Zhao, T.; Wang, F.; Xu, J.; Xue, B. Palladium Nanoparticles Supported on Exfoliated g-C_3N_4 as Efficient Catalysts for Selective Oxidation of Benzyl Alcohol by Molecular Oxygen. *New J. Chem.* **2021**, *45*, 13519–13528. [CrossRef]
24. Bojdys, M.J.; Müller, J.-O.; Antonietti, M.; Thomas, A. Ionothermal synthesis of crystalline, condensed, graphitic carbon nitride. *Chem. Eur. J.* **2008**, *14*, 8177–8182. [CrossRef]
25. Zhang, Y.; Mori, T.; Ye, J. Polymeric Carbon Nitrides: Semiconducting Properties and Emerging Applications in Photocatalysis and Photoelectrochemical Energy Conversion. *Sci. Adv. Mater.* **2012**, *4*, 282–291. [CrossRef]
26. Thomas, A.; Fischer, A.; Goettmann, F.; Antonietti, M.; Müller, J.-O.; Schlögl, R.; Carlsson, J.M. Graphitic carbon nitride materials: Variation of structure and morphology and their use as metal-free catalysts. *J. Mater. Chem.* **2008**, *18*, 4893–4908. [CrossRef]
27. Xu, J.; Wu, H.-T.; Wang, X.; Xue, B.; Li, Y.-X.; Cao, Y. A new and environmentally benign precursor for the synthesis of mesoporous g-C_3N_4 with tunable surface area. *Phys. Chem. Chem. Phys.* **2013**, *15*, 4510–4517. [CrossRef]
28. Shi, S.; Chen, C.; Wang, M.; Ma, J.; Gao, J.; Xu, J. Mesoporous strong base supported cobalt oxide as a catalyst for the oxidation of ethylbenzene. *Catal. Sci. Technol.* **2014**, *4*, 3606–3610. [CrossRef]
29. Jie, S.; Yang, C.; Chen, Y.; Liu, Z. Facile synthesis of ultra-stable Co-N-C catalysts using cobalt porphyrin and peptides as precursors for selective oxidation of ethylbenzene. *Mol. Catal.* **2018**, *458*, 1–8. [CrossRef]
30. Jie, S.; Lin, X.; Chao, Z.; Liu, Z. Effective ternary copper-cerium-cobalt catalysts synthesized via a modified pechini method for selective oxidation of ethylbenzene. *Mater. Chem. Phys.* **2018**, *214*, 239–246. [CrossRef]
31. Jiang, Y.; Zhang, C.; Li, Y.; Jiang, P.; Jiang, J.; Leng, Y. Solvent-free aerobic selective oxidation of hydrocarbons catalyzed by porous graphitic carbon encapsulated cobalt composites. *New J. Chem.* **2018**, *42*, 16829–16835. [CrossRef]
32. Gao, L.; Zhuge, W.; Feng, X.; Sun, W.; Sun, X.; Zheng, G. Co/rGO synthesized via the alcohol-thermal method as a heterogeneous catalyst for the highly efficient oxidation of ethylbenzene with oxygen. *New J. Chem.* **2019**, *43*, 8189–8194. [CrossRef]
33. Fu, L.; Chen, Y.; Zhao, S.; Liu, Z.; Zhu, R. Sulfur-mediated synthesis of N-doped carbon supported cobalt catalysts derived from cobalt porphyrin for ethylbenzene oxidation. *RSC Adv.* **2016**, *6*, 19482–19491. [CrossRef]
34. Zhang, L.; Jie, S.; Liu, Z. Bicontinuous mesoporous Co, N co-doped carbon catalysts with high catalytic performance for ethylbenzene oxidation. *New J. Chem.* **2019**, *43*, 7275–7281. [CrossRef]
35. Oh, Y.; Hwang, J.O.; Lee, E.; Yoon, M.; Le, V.; Kim, Y.; Kim, D.H.; Kim, S.O. Divalent Fe Atom Coordination in Two-Dimensional Microporous Graphitic Carbon Nitride. *ACS Appl. Mater. Interfaces* **2016**, *8*, 25438–25443. [CrossRef]
36. Su, Q.; Sun, J.; Wang, J.; Yang, Z.; Cheng, W.; Zhang, S. Urea-derived graphitic carbon nitride as an efficient heterogeneous catalyst for CO_2 conversion into cyclic carbonates. *Catal. Sci. Technol.* **2014**, *4*, 1556–1562. [CrossRef]
37. Yu, Z.-H.; Gan, Y.-L.; Xu, J.; Xue, B. Direct Catalytic Hydroxylation of Benzene to Phenol Catalyzed by $FeCl_3$ Supported on Exfoliated Graphitic Carbon Nitride. *Catal. Lett.* **2020**, *150*, 301–311. [CrossRef]
38. Zhu, J.; Wei, Y.; Chen, W.; Zhao, Z.; Thomas, A. Graphitic carbon nitride as a metal-free catalyst for NO decomposition. *Chem. Commun.* **2010**, *46*, 6965–6967. [CrossRef]
39. Bahuguna, A.; Kumar, A.; Chhabra, T.; Kumar, A.; Krishnan, V. Potassium-Functionalized Graphitic Carbon Nitride Supported on Reduced Graphene Oxide as a Sustainable Catalyst for Knoevenagel Condensation. *ACS Appl. Nano Mater.* **2018**, *1*, 6711–6723. [CrossRef]
40. Xu, J.; Long, K.-Z.; Wang, Y.; Xue, B.; Li, Y.-X. Fast and facile preparation of metal-doped g-C_3N_4 composites for catalytic synthesis of dimethyl carbonate. *Appl. Catal. A* **2015**, *496*, 1–8. [CrossRef]
41. Chen, P.-W.; Li, K.; Yu, Y.-X.; Zhang, W.-D. Cobalt-doped graphitic carbon nitride photocatalysts with high activity for hydrogen evolution. *Appl. Sur. Sci.* **2017**, *392*, 608–615. [CrossRef]
42. Yue, B.; Li, Q.; Iwai, H.; Kako, T.; Ye, J. Hydrogen production using zinc-doped carbon nitride catalyst irradiated with visible light. *Sci. Technol. Adv. Mater.* **2011**, *12*, 034401. [CrossRef] [PubMed]
43. Yang, C.; Jie, S.; Zhu, R.; Zhang, N.; Wang, J.; Liu, Z. Co-N-C Catalysts Synthesized via Pyrolyzing the Ionic Liquids Solution Dissolved with Casein and Cobalt Porphyrin for Ethylbenzene Oxidation. *ChemistrySelect* **2017**, *2*, 4255–4260. [CrossRef]
44. Imran, G.; Maheswari, R. Mn-incorporated SBA-1 cubic mesoporous silicates: Synthesis and characterization. *Mater. Chem. Phys.* **2015**, *161*, 237–242. [CrossRef]
45. Pachamuthu, M.P.; Rajalakshmi, R.; Maheswari, R.; Ramanathan, A. Direct glycol assisted synthesis of an amorphous mesoporous silicate with framework incorporated Co2+: Characterization and catalytic application in ethylbenzene oxidation. *RSC Adv.* **2014**, *4*, 29909–29916. [CrossRef]

46. Habibi, D.; Faraji, A.R.; Arshadi, M.; Fierro, J.L.G. Characterization and catalytic activity of a novel Fe nano-catalyst as efficient heterogeneous catalyst for selective oxidation of ethylbenzene, cyclohexene, and benzylalcohol. *J. Mol. Catal. A* **2013**, *372*, 90–99. [CrossRef]
47. Kalita, L.; Saikia, L. Palladium-Supported Nanoceria: A Highly Efficient Catalyst for Solvent-Free Selective Oxidation of Ethylbenzene to Acetophenone. *ChemistrySelect* **2020**, *5*, 4848–4855. [CrossRef]
48. Goettmann, F.; Fischer, A.; Antonietti, M.; Thomas, A. Chemical synthesis of mesoporous carbon nitrides using hard templates and their use as a metal-free catalyst for Friedel-Crafts reaction of benzene. *Angew. Chem. Int. Ed.* **2006**, *45*, 4467–4471. [CrossRef]